

## Development of an adaptive CTM–RPIM method for modeling large deformation problems in geotechnical engineering

Li, Jianguo; Wang, Bin; Jiang, Quan; He, Benguo; Zhang, Xue; Vardon, Philip J.

**DOI**

[10.1007/s11440-021-01416-1](https://doi.org/10.1007/s11440-021-01416-1)

**Publication date**

2021

**Document Version**

Final published version

**Published in**

Acta Geotechnica

**Citation (APA)**

Li, J., Wang, B., Jiang, Q., He, B., Zhang, X., & Vardon, P. J. (2021). Development of an adaptive CTM–RPIM method for modeling large deformation problems in geotechnical engineering. *Acta Geotechnica*, 17(6), 2059–2077. <https://doi.org/10.1007/s11440-021-01416-1>

**Important note**

To cite this publication, please use the final published version (if applicable). Please check the document version above.

**Copyright**

Other than for strictly personal use, it is not permitted to download, forward or distribute the text or part of it, without the consent of the author(s) and/or copyright holder(s), unless the work is under an open content license such as Creative Commons.

**Takedown policy**

Please contact us and provide details if you believe this document breaches copyrights. We will remove access to the work immediately and investigate your claim.

***Green Open Access added to TU Delft Institutional Repository***

***'You share, we take care!' - Taverne project***

**<https://www.openaccess.nl/en/you-share-we-take-care>**

Otherwise as indicated in the copyright section: the publisher is the copyright holder of this work and the author uses the Dutch legislation to make this work public.



# Development of an adaptive CTM–RPIM method for modeling large deformation problems in geotechnical engineering

Jianguo Li<sup>1,2</sup> · Bin Wang<sup>1,2</sup> · Quan Jiang<sup>1,2</sup> · Benguo He<sup>3</sup> · Xue Zhang<sup>4</sup> · Philip J. Vardon<sup>5</sup>

Received: 3 July 2021 / Accepted: 9 November 2021

© The Author(s), under exclusive licence to Springer-Verlag GmbH Germany, part of Springer Nature 2021

## Abstract

In this paper, a meshfree method called adaptive CTM–RPIM is developed to model geotechnical problems with large deformation. The developed adaptive CTM–RPIM is a combination of the Cartesian transformation method (CTM), the radial point interpolation method (RPIM) and the alpha shape method. To reduce the requirement for meshes, the CTM is adopted to transform domain integrals into line integrals, and the RPIM is applied to construct interpolation functions. The alpha shape method, which is capable of capturing severe boundary evolution due to large deformations, is then introduced into the CTM–RPIM to form the adaptive CTM–RPIM. The accuracy of CTM–RPIM is first verified by considering a cantilever beam under small deformation, where the influence of key parameters on the simulation results is explored. Afterward, the ability of the adaptive CTM–RPIM to handle large deformation problems is demonstrated by simulating cantilever beams with large deformations for which analytical solutions are available. Finally, the ability of the proposed method to model the geotechnical large deformations is illustrated from both quasi-static and dynamic aspects, where a slope failure problem and a footing bearing capacity problem are modeled to evaluate the stability of geotechnical structures; and a 2-D soil collapse experiment using small aluminum bars is simulated to show the method capability in describing the soil flows. These benchmark examples demonstrate that the adaptive CTM–RPIM is a numerical method with broad application prospects for modeling large deformation problems in geotechnical engineering.

**Keywords** Alpha shape method · Cartesian transformation method · Geotechnical engineering · Large deformation · Radial point interpolation method

✉ Bin Wang  
bwang@whrsm.ac.cn

✉ Quan Jiang  
qjiang@whrsm.ac.cn

<sup>1</sup> State Key Laboratory of Geomechanics and Geotechnical Engineering, Institute of Rock and Soil Mechanics, Chinese Academy of Sciences, Wuhan, China

<sup>2</sup> University of Chinese Academy of Sciences, Beijing, China

<sup>3</sup> Key Laboratory of Ministry of Education on Safe Mining of Deep Metal Mines, Northeastern University, Shenyang, China

<sup>4</sup> Department of Civil Engineering and Industrial Design, University of Liverpool, Liverpool, UK

<sup>5</sup> Geo-Engineering Section, Delft University of Technology, Delft, The Netherlands

## 1 Introduction

The occurrence of many natural disasters, such as landslides, earthquakes, and debris flows, is often accompanied by large and severe deformations [8, 11, 18]. Many numerical methods have been developed to solve these problems, but some of them encounter problems such as mesh entanglement and inconsistency between the integral domain and problem domain.

When dealing with large deformation problems, some mesh-based methods such as the finite element method (FEM) [2, 7] and the finite difference method (FDM) [21, 26] require a time-consuming operation, i.e., remeshing, to avoid mesh distortions. To overcome the mesh reliability problem, various meshfree methods have been developed. However, a background mesh is used in some classical meshfree methods to facilitate the integration of the stiffness matrix and force vector. Using the material

point method (MPM) [3, 14] and the element-free Galerkin method (EFGM) [12, 24, 28] as examples, the use of a background mesh results in an inconsistency between the integral domain and the problem domain. This inconsistency may cause errors when the model is rough. In addition, a problem in MPM may arise and increase the computational cost; that is, at each step, the user must judge which background cell the integral point is located in. Some other meshfree methods that do not use a background mesh may also encounter minor disadvantages, such as the meshfree local Petrov–Galerkin method (MLPG) [1]. In the MLPG, the weak form of the governing equation is established by the local Petrov–Galerkin method, which may lead to asymmetry in the stiffness matrix and increase the computational time. In summary, a meshfree method without a background mesh that uses the Galerkin method to construct its weak form and includes both a coincident problem domain and an integral domain can be developed to avoid these disadvantages.

The Cartesian transformation method (CTM) [4, 31], which originates from the boundary element method (BEM) [10], is an integral method that can transform domain integration into a boundary integration and a 1-D integration. This strategy does not require a mesh or background mesh when computing the integration of the stiffness matrix and force vector, and the integral domain coincides with the problem domain. The radial point interpolation method (RPIM) [9, 15, 17] is of high precision for scattered data interpolation, and it can eliminate the mesh restriction when constructing the shape functions. Moreover, the RPIM has a simple theoretical basis that is easy to implement programmatically and extend to 3-D space. It is conceivable that the combination of the CTM and RPIM in the governing equation based on the Galerkin method would result in a meshfree method with a symmetrical stiffness matrix, and a coincident problem domain and integral domain. Another problem in dealing with geotechnical large deformation problems is tracking the boundary of the problem domain when severe deformations occur. An external algorithm, the alpha shape method [32] is incorporated, and this addition allows the accurate tracking of the boundary during the dynamic large deformation process. The reliability of the alpha shape method has already been proven in the particle finite element method (PFEM) [22] and smooth particle finite element method (SPFEM) [13, 20, 34], in which the alpha shape method is used to identify the boundary with a Delaunay triangularization. The adaptive procedure can be constructed by tracking the boundary as the deformation grows. Notably, boundary identification may be avoided via the use of CTM integration in regular regions inside the object and nodal integrations outside this region, as seen in

the EFGM [27], and this can be further investigated in the future.

Therefore, with the motivation of developing a meshfree method without a background mesh, which uses the Galerkin method to construct its weak form and includes a coincident problem domain and integral domain, an adaptive CTM–RPIM is formulated. This strategy combines the CTM, RPIM and alpha shape method. The proposed method, on one hand, inherits the advantages of the RPIM method and its ability to model large deformations; on the other hand, by utilizing the CTM integration algorithm, the numerical stability can be improved in a relatively convenient way, i.e., transferring the domain integration into the line integrals.

The entire paper is primarily organized into three parts. Firstly, a brief introduction to the adaptive CTM–RPIM is provided, and the formulation of the CTM and RPIM as well as the alpha shape method is then presented. The key parameters of the CTM and RPIM are studied in terms of their computational accuracies, and the optimal parameters are determined and suggested. Secondly, two large deformation examples involving cantilever beams are executed to verify the advantages of this method for large deformation problems. Finally, three geotechnical examples, including slope stability, foundation bearing capacity and soil flow, are shown, and the reliability of the method is thoroughly demonstrated.

## 2 Formulation and implementation procedure of the adaptive CTM–RPIM

A detailed introduction to the development of the adaptive CTM–RPIM is presented in this section. The governing equation and implementation procedure for the adaptive CTM–RPIM are provided. After that, the computational steps for programming are presented, and they include both the quasi-static version and dynamic version. Finally, the formulations of the CTM, the construction of the RPIM shape functions and the procedure of the alpha shape method are illustrated in detail.

### 2.1 Implementation procedure of the adaptive CTM–RPIM

#### 2.1.1 The governing equation

The mechanical behavior of soil usually obeys the governing equation of continuum mechanics, which can be derived from the momentum conservation equation.

$$\nabla \boldsymbol{\sigma} + \mathbf{b} = \rho \ddot{\mathbf{u}} \quad (1)$$

where  $\nabla$  is the partial differential operator,  $\sigma$  is the stress vector,  $b$  is the boundary condition,  $\rho$  is the density of the material, and  $\ddot{u}$  is the acceleration.

To solve this partial differential equation (PDE), the Galerkin method can be used in its weak form by introducing a test function  $\delta u$  into Eq. (1).

$$\int_{\Omega} \delta u : \sigma d\Omega - \int_{\Omega} \delta u \cdot f^b d\Omega - \int_{\Gamma} \delta u \cdot f^{\Gamma} d\Gamma = \int_{\Omega} \delta u \cdot \rho \ddot{u} d\Omega \tag{2}$$

where  $f^b$  is the body force, and  $f^{\Gamma}$  is the surface force. The above equation is a conservation equation of virtual energy. The first term on the left-hand side is caused by an internal force, the second and third terms are caused by an external force, and the term on the right-hand side is caused by inertia force.

To solve Eq. (2), the discrete form can be constructed similarly as in the standard FEM, and the adaptive procedure is established to address large deformation problems. These procedures will be provided in the next three sections.

### 2.1.2 Adaptive procedure for large deformations

The strategy used to combine the alpha shape method, CTM and RPIM to construct an adaptive procedure that can be automatically executed during large deformations is explained in this section. In this procedure, the CTM–RPIM is used to establish the discrete form of the momentum conservation equation, and the alpha shape method is used to track the boundary when the configuration is updated. A simple schematic diagram is depicted in Fig. 1.

As shown in Fig. 1, the adaptive CTM–RPIM for large deformation analysis can be divided into four basic steps:

- (1) Search the boundary of the field node cloud to determine the scope of the problem domain and integral domain.
- (2) Generate integral lines and integral points and form the stiffness matrix, mass matrix and force vector.
- (3) Apply boundary conditions to establish the discretized governing equation to be solved.
- (4) Solve the governing equation formed in step (3) and then delete the previous boundary. The problem domain returns to the state represented by the field nodes.

The above four steps are repeated until the error of displacement, force, or energy between two adjacent steps is tolerable.

Note that the remesh operation is not required by the proposed adaptive CTM–RPIM. Only boundary identification is carried out using the alpha shape method, so there are no problems caused by mesh distortion. Moreover, the integral domain is consistent with the problem domain, which is helpful for accuracy. Additionally, in contrast to the EFGM and the traditional RPIM, there is no need to check whether the integral points are in the problem domain. Furthermore, compared with MPM, there is no need to determine which background cell an integral point is in.

### 2.1.3 Computational steps for quasi-static problems

For quasi-static problems, the acceleration can be ignored so that the right-hand term of Eq. (2) is eliminated. The governing equation can be rewritten as,

$$\int_{\Omega} \delta u : \sigma d\Omega = \int_{\Omega} \delta u \cdot f^b d\Omega + \int_{\Gamma} \delta u \cdot f^{\Gamma} d\Gamma \tag{3}$$

This form is commonly found in the standard FEM, which can become discrete by assuming that there is a relationship between the variables of the concerned point and the variables on the field nodes that use shape functions. Following a similar process to the standard FEM, the discretized global equilibrium equation can be derived as,

$$KU = F_{\text{ext}} \tag{4}$$

where  $K$  is the global stiffness matrix, and  $F_{\text{ext}}$  is the global external force vector. Using CTM integration, a detailed expression of each term can be obtained.

$$K = \sum_{i=1}^m B_i^T D_i B_i w_i^x w_i^y J_i^x J_i^y \tag{5}$$

$$F_{\text{ext}} = \sum_{i=1}^m N_i f_i^b w_i^x w_i^y J_i^x J_i^y + \sum_{j=1}^{mb} N_j f_j^{\Gamma} w_j J_j \tag{6}$$

where  $m$  is the number of integral points;  $B_i$  is the matrix of the partial derivative of the shape functions at the  $i$ th integral point;  $N_i$  is the RPIM shape function matrix at the  $i$ th integral point; and  $w_i^x$ ,  $w_i^y$ ,  $J_i^x$ , and  $J_i^y$  are the weight and Jacobi determinant in the  $x$  and  $y$  directions of the  $i$ th integral point. The second term in  $F_{\text{ext}}$  has a similar meaning, except that it is in the form of a boundary integration, which can be solved using the Gaussian integral method.

Moreover, the expression of the internal force, which is another expression of  $KU$  in Eq. (4), can also be derived from the left-hand term of Eq. (3).

$$F_{\text{int}} = \sum_{i=1}^m B_i \sigma_i w_i^x w_i^y J_i^x J_i^y \tag{7}$$

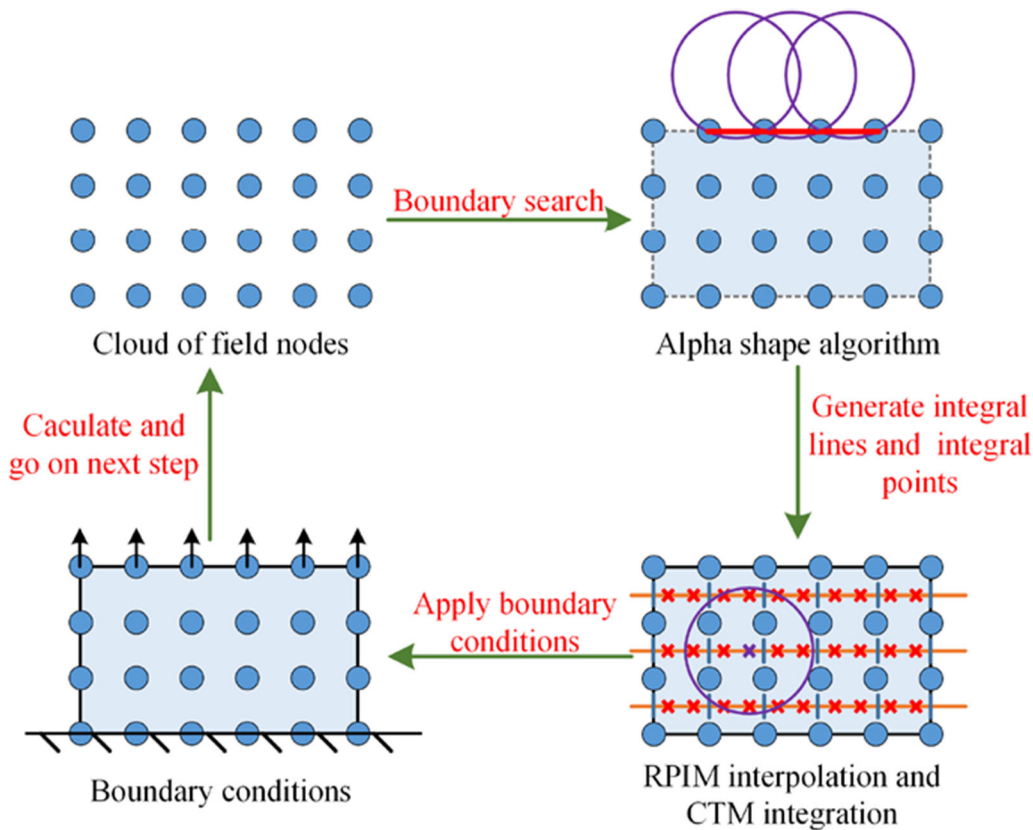


Fig. 1 The adaptive CTM–RPIM implementation procedure

To solve Eq. (4), Newton–Raphson iteration is often used. The quasi-static version of adaptive CTM–RPIM is provided here for a material nonlinearity example with small deformation or a weightless material with large deformation. The adaptive procedure is as follows:

- (1) Discretize the problem domain using a series of field nodes.
- (2) Loop over the incremental step ( $n$ th incremental step).
- (3) Search the boundary of the problem domain based on the field node cloud using the alpha shape method.
- (4) Generate the integral lines and integral points and form the total external force vector  $\mathbf{F}_{\text{ext}}^n$  for the present incremental step.
- (5) Loop over the Newton–Raphson iteration ( $l$ th iteration step).
- (6) Form the global stiffness matrix  $\mathbf{K}_l^n$  and the global internal force vector  $\mathbf{F}_{\text{int}(l)}^n$ .
- (7) Solve the governing equation  $\mathbf{K}_l^n \mathbf{U}_l^n = \mathbf{F}_{\text{ext}}^n - \mathbf{F}_{\text{int}(l)}^n$ .
- (8) Check convergence.
  - If the problem has converged, go to step 10.
- (9) End looping of the Newton–Raphson iteration.

- (10) Check the incremental step limit.
  - If the incremental step is greater than the limit, update the configuration and go to step (12).
  - If the incremental step is less than the limit, update the configuration and go to step (2).
- (11) End looping of the incremental step.
- (12) Post-processing.

#### 2.1.4 Computational steps for dynamic problems

For dynamic problems, if weight is accounted for, the acceleration cannot be ignored. The left and right hands of Eq. (2) can be swapped to make the equation more suitable for constructing the time integral format.

$$\int_{\Omega} \delta \mathbf{u} \cdot \rho \ddot{\mathbf{u}} d\Omega = \int_{\Omega} \delta \mathbf{u} : \boldsymbol{\sigma} d\Omega - \int_{\Omega} \delta \mathbf{u} \cdot \mathbf{f}^b d\Omega - \int_{\Gamma} \delta \mathbf{u} \cdot \mathbf{f}^{\Gamma} d\Gamma \quad (8)$$

Similar to the standard FEM, discrete momentum conservation can be derived from Eq. (8).

$$\mathbf{M}\ddot{\mathbf{U}} = \mathbf{F}_{\text{ext}} - \mathbf{F}_{\text{int}} \quad (9)$$

where  $\mathbf{M}$  is the mass matrix, and  $\ddot{\mathbf{U}}$  is the acceleration vector. The lumped matrix is used here to improve the computational efficiency.

Sometimes, damping force can be introduced into Eq. (9) for the convergence rate and stability of the program, i.e.,

$$\mathbf{M}\ddot{\mathbf{U}} = \mathbf{F}_{\text{ext}} - \mathbf{F}_{\text{int}} + \mathbf{F}_{\text{damp}} \tag{10}$$

where  $\mathbf{F}_{\text{damp}}$  is the damping force vector. If local damping is used, this vector can be expressed as follows:

$$\mathbf{F}_{\text{damp}} = -f|\mathbf{F}_{\text{ext}} - \mathbf{F}_{\text{int}}|\text{sign}(\dot{\mathbf{U}}) \tag{11}$$

where  $f$  is the damping factor, and  $\dot{\mathbf{U}}$  is the velocity vector, which can be determined using the central difference method.

For dynamic problems with both geometric nonlinearity and material nonlinearity, the detailed procedures with explicit time integrals are provided as follows:

- (1) Discretize the problem domain using a series of field nodes.
- (2) Start time step  $n$ .
- (3) Track the boundary using the alpha shape method.
- (4) Generate the integral lines and integral points.
  - A. compute the total force vector at time  $t^n$ :  $\mathbf{F}^n = \mathbf{F}_{\text{ext}}^n - \mathbf{F}_{\text{int}}^n + \mathbf{F}_{\text{damp}}^n$ .
  - B. compute the mass matrix at time  $t^n$ :  $\mathbf{M}^n$ .
- (5) Calculate the acceleration vector at time  $t^n$ :  $\ddot{\mathbf{U}}^n = (\mathbf{M}^n)^{-1}\mathbf{F}^n$ .
- (6) Calculate the velocity vector at time  $t^{n+1/2}$ :  $\dot{\mathbf{U}}^{n+1/2} = \dot{\mathbf{U}}^{n-1/2} + \Delta t^n \ddot{\mathbf{U}}^n$ , where  $\Delta t^n = t^{n+1/2} - t^{n-1/2}$ .
- (7) Calculate the displacement vector at time  $t^{n+1}$ :  $\mathbf{U}^{n+1} = \mathbf{U}^n + \Delta t^{n+1/2} \dot{\mathbf{U}}^{n+1/2}$ , where  $\Delta t^{n+1/2} = t^{n+1} - t^n$ .
- (8) Calculate the internal force vector at time  $t^{n+1}$ :  $\mathbf{F}_{\text{int}}^{n+1}$ .
- (9) Update the configuration using the displacement vector  $\mathbf{U}^{n+1}$ .
- (10) Check convergence or the check limit.

If the problem has converged or reached the time step limit, end the calculation; otherwise, go to step (2) and start the  $n + 1$  time step.

### 2.2 Formulation of CTM

The CTM is a special integration method originally applied in BEM [10]. Here, it is introduced into the meshfree method to form the stiffness matrix, mass matrix and force

vector. Consider an integration  $I_{\text{in}}$  of a function  $f_{\text{in}}(x, y)$  over a domain  $\Omega_{\text{in}}$

$$I_{\text{in}} = \int_{\Omega_{\text{in}}} f_{\text{in}}(x, y) dx dy \tag{12}$$

As shown in Fig. 2, the domain is so complex that the integration cannot be directly executed. To solve Eq. (12), a rectangular auxiliary domain  $\Omega_{\text{all}}$  that fully contains the domain over which the integration must take place is constructed. The function in the rectangular auxiliary domain,  $f_{\text{all}}(x, y)$ , can then be expressed as

$$f_{\text{all}}(x, y) = \begin{cases} f_{\text{in}}(x, y) & (\text{in } \Omega_{\text{in}}) \\ 0 & (\text{out of } \Omega_{\text{in}}) \end{cases} \tag{13}$$

The integration  $I_{\text{in}}$  is rewritten as

$$I_{\text{in}} = \int_{\Omega_{\text{all}}} f_{\text{all}}(x, y) dx dy \tag{14}$$

Assuming that the function  $h_{\text{all}}(x, y)$  is the integration of  $f_{\text{all}}(\xi, y)$

$$h_{\text{all}}(x, y) = \int_c^x f_{\text{all}}(\xi, y) d\xi \tag{15}$$

where  $\xi$  is a variable independent of  $x$  and  $y$ , and  $c$  is an arbitrary constant. By adopting Green's theorem, Eq. (14) can be expressed as

$$\begin{aligned} I_{\text{in}} &= \int_{\Gamma_{\text{all}}} h_{\text{all}}(x, y) dy \\ &= \int_{\Gamma_{\text{all}}} \left( \int_c^x f_{\text{all}}(\xi, y) d\xi \right) dy \\ &= \int_{\Gamma_{AB+BC+CD+DA}} \left( \int_c^x f_{\text{all}}(\xi, y) d\xi \right) dy \end{aligned} \tag{16}$$

For a rectangular auxiliary domain  $\Omega_{\text{all}}$ ,  $dy$  is zero on boundaries  $DA$  and  $BC$ . By setting  $c$  to  $u_x$ ,  $\int_c^x f_{\text{all}}(\xi, y) d\xi$  is

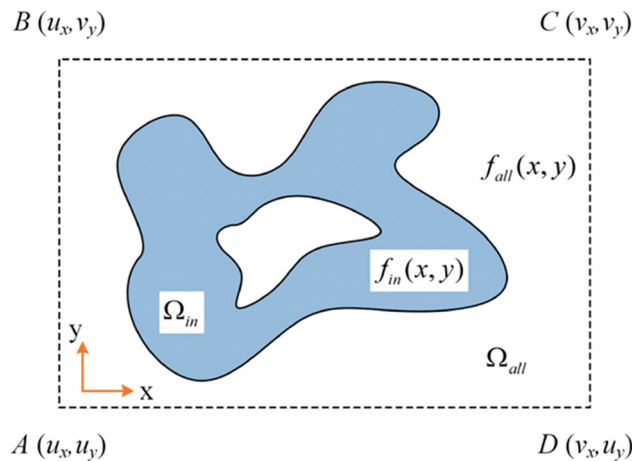


Fig. 2 Domain integration of the function  $f_{\text{in}}(x, y)$

zero on boundary  $AB$ , implying that the integration in Eq. (16) only needs to be calculated on boundary  $CD$ .

$$\begin{aligned} I_{\text{in}} &= \int_{\Gamma_{\text{CD}}} \left( \int_{u_x}^{x} f_{\text{all}}(\xi, y) d\xi \right) dy \\ &= \int_{\Gamma_{\text{CD}}} \left( \int_{u_x}^{v_x} f_{\text{all}}(\xi, y) d\xi \right) dy \\ &= \int_{u_y}^{v_y} \left( \int_{u_x}^{v_x} f_{\text{all}}(x, y) dx \right) dy \end{aligned} \quad (17)$$

The above integration can be divided as follows:

$$I_{\text{in}} = \int_{u_y}^{v_y} g(y) dy \quad (18)$$

$$g(y) = \int_{u_x}^{v_x} f_{\text{all}}(x, y) dx \quad (19)$$

To calculate these two integrations, a series of integral lines are introduced, as shown in Fig. 3. Then, the integration  $I_{\text{in}}$  can be evaluated based on some numerical integration methods, such as Gauss integration, and the value of the  $i$ th integral line is  $g(y_i)$ .

By dividing the  $i$ th integral line into  $n - 1$  segments,  $g(y_i)$  can be calculated as

$$\begin{aligned} g(y_i) &= \int_{x_1}^{x_n} f_{\text{all}}(x, y_i) dx \\ &= \sum_{j=2}^n \left( \int_{x_{j-1}}^{x_j} f_{\text{all}}(x, y_i) dx \right) \end{aligned} \quad (20)$$

Recalling the relationship between  $f_{\text{all}}$  and  $f_{\text{in}}$ ,  $g(y_i)$  can also be expressed in terms of  $f_{\text{in}}$ . If  $f_{\text{in}}$  is used, the integration  $\int_{x_4}^{x_5} f_{\text{in}}(x, y_i) dx$  vanishes in Fig. 3 and  $g(y_i)$  is written as

$$g(y_i) = \sum_{j=2}^n \left( \int_{x_{j-1}}^{x_j} f_{\text{in}}(x, y_i) dx \right) \quad (j \neq 5) \quad (21)$$

Similar to the evaluation of  $I_{\text{in}}$ ,  $g(y_i)$  can be calculated numerically. Using the Gauss integration scheme, we obtain

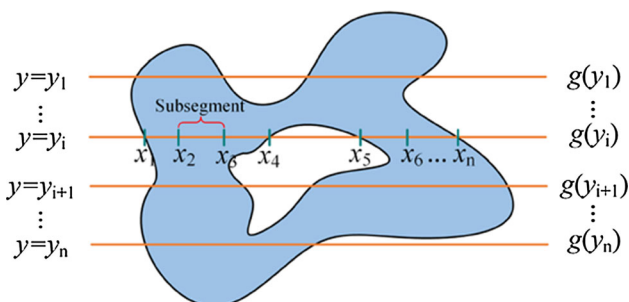


Fig. 3 CTM integral scheme

$$I_{\text{in}} = \sum_{i=1}^{m_y} g(y_i) \cdot w_i^y \cdot J_i^y \quad (22)$$

where  $m_y$  represents the total number of integral lines;  $w_i^y$  and  $J_i^y$  are the weight and Jacobi determinant along the  $y$ -direction, respectively, and

$$g(y_i) = \sum_{j_x=1}^{m_x} f_{\text{in}}(x_{j_x}, y_i) \cdot w_{j_x}^x \cdot J_{j_x}^x \quad (23)$$

where  $m_x$  is the total number of integral points on each integral line, and  $w_{j_x}^x$  and  $J_{j_x}^x$  are the weight and Jacobi determinant along the  $x$ -direction, respectively.

Substituting Eq. (23) into (22) leads to the final form of  $I_{\text{in}}$

$$I_{\text{in}} = \sum_{k=1}^m f_{\text{in}}(x_k, y_k) \cdot w_k^x \cdot w_k^y \cdot J_k^x \cdot J_k^y \quad (24)$$

which is the sum of the product of the function at the integral points and the corresponding weight and Jacobi determinant in two directions.  $k$  is the global number of integral points, and  $m$  is the total number of integral points. As such, the CTM transforms domain integration into line integration. Consequently, only the intersections of integral lines and boundaries are needed during the simulation, which leads to a purely meshfree method with a coincident problem domain and integral domain. Equation (24) is the exact numerical integration method used in Sect. 2.1 to calculate the stiffness matrix, mass matrix and force vector.

### 2.3 RPIM-based shape functions

Generally, in meshfree methods, the problem domain is represented by a series of field nodes. Because of the adoption of the CTM, there is no background mesh, and thus, the shape functions should be constructed based on the field nodes. In this paper, the RPIM is used for this purpose, which is introduced below.

For an arbitrary integral point, a support domain can be formed, as shown in Fig. 4. The shape of the support domain can be circular or rectangular. Supposing that the

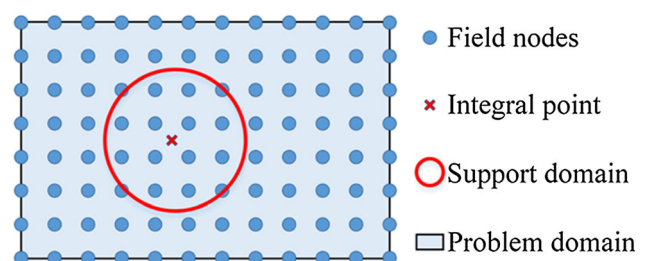


Fig. 4 Support domain in the RPIM

support domain covers  $n$  field nodes, the field variable  $F(x, y)$  at the concerned point can be approximated by

$$F(x, y) = [R^T(r(x, y)) \quad P^T(x, y)] \begin{bmatrix} A \\ B \end{bmatrix} \tag{25}$$

where  $R^T(r(x, y)) = [r_1(x, y) \quad r_2(x, y) \quad \dots \quad r_n(x, y)]$  is the vector consisting of the radial basis function (RBF) with  $r_i(x, y)$  being the distance between the point at  $(x, y)$  and the field node at  $(x_i, y_i)$  in two-dimensional cases,

$$P^T(x, y) = [1 \quad x \quad y \quad xy \quad x^2 \quad y^2 \quad \dots]$$

is the vector of polynomial basis functions, and  $A$  and  $B$  are row vectors of constants to be determined. Equation (25) must be satisfied at all field nodes. For example, the field variable at  $j$ th field node  $(x_j, y_j)$  is

$$F(x_j, y_j) = [R^T(r(x_j, y_j)) \quad P^T(x_j, y_j)] \begin{bmatrix} A \\ B \end{bmatrix} \tag{26}$$

By assembling the above equation for all field nodes, the following matrix form is obtained

$$F_0 = R_0^T A + P_0^T B \tag{27}$$

The detailed forms of  $R_0$ ,  $P_0$  and vector  $F_0$  are expressed as follows

$$F_0 = [F(x_1, y_1) \quad F(x_2, y_2) \quad \dots \quad F(x_n, y_n)]^T \tag{28}$$

$$R_0^T = \begin{bmatrix} r_1(x_1, y_1) & r_2(x_1, y_1) & \dots & r_n(x_1, y_1) \\ r_1(x_2, y_2) & r_2(x_2, y_2) & \dots & r_n(x_2, y_2) \\ \vdots & \vdots & \ddots & \vdots \\ r_1(x_n, y_n) & r_2(x_n, y_n) & \dots & r_n(x_n, y_n) \end{bmatrix} \tag{29}$$

$$P_0 = \begin{bmatrix} 1 & 1 & \dots & 1 \\ x_1 & x_2 & \dots & x_n \\ y_1 & y_2 & \dots & y_n \\ \vdots & \vdots & \vdots & \vdots \end{bmatrix} \tag{30}$$

Note that if there are  $n$  field nodes in the support domain and an  $m$ -term polynomial basis is used, there are  $m + n$  unknowns in vectors  $A$  and  $B$ . To ensure that the solution to Eq. (27) is unique, the following constraint is assumed

$$P_0 A = 0 \tag{31}$$

With this constraint, Eq. (27) can be enriched as

$$\begin{bmatrix} F_0 \\ 0 \end{bmatrix} = \begin{bmatrix} R_0^T & P_0^T \\ P_0 & 0 \end{bmatrix} \begin{bmatrix} A \\ B \end{bmatrix} \tag{32}$$

By solving  $A$  and  $B$  from Eq. (32) and substituting them into Eq. (25), we obtain the expression of  $F(x, y)$ , which is

$$F(x, y) = [R^T(r(x, y)) \quad P^T(x, y)] \begin{bmatrix} R_0^T & P_0^T \\ P_0 & 0 \end{bmatrix}^{-1} \begin{bmatrix} F_0 \\ 0 \end{bmatrix} \tag{33}$$

The first  $n$  terms of

$$[R^T(r(x, y)) \quad P^T(x, y)] \begin{bmatrix} R_0^T & P_0^T \\ P_0 & 0 \end{bmatrix}^{-1}$$

are the RPIM shape functions for the field nodes in the support domain, which can be used to construct interpolation functions for the integral point.

There are different types of RBFs, such as multiquadrics (MQ), Gaussian (EXP), thin-plate splines (TPS) and logarithmic RBFs. For simplicity, the TPS RBF

$$R(x, y) = r(x, y)^\eta \tag{34}$$

is used in this paper, where  $\eta$  is the shape parameter.

### 2.4 Alpha shape method for tracking the boundary

As indicated in Sects. 2.2 and 2.3, a series of field nodes whose boundary is known at the undeformed configuration is generated first if the CTM–RPIM is used. However, when the object undergoes large deformation, the boundary will evolve accordingly. Therefore, an efficient boundary identification method is essential. In this paper, the alpha shape method is adopted for boundary identification.

The basic idea of the alpha shape method is to check whether there is an empty circle of radius  $\alpha$  passing through any two field nodes. If such a circle exists, the segment connecting the two field nodes is a boundary segment. The method can be implemented as follows (see Fig. 5):

- (1) Calculate the length of line segment  $P_1P_2$ , which consists of any two field nodes  $P_1$  and  $P_2$ .
- (2) Compare the length of  $P_1P_2$  with the preset circle diameter  $2\alpha$ .
- (3) If  $P_1P_2$  is less than  $2\alpha$ , draw two circles  $\odot O_1$  and  $\odot O_2$  with radius  $\alpha$  passing through  $P_1$  and  $P_2$ .

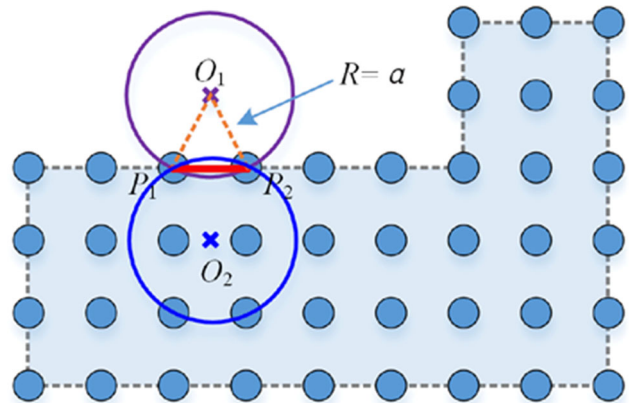


Fig. 5 Schematic diagram of the alpha shape method

- (4) If either circle is empty or with other nodes on the circle, line  $P_1P_2$  is treated as a boundary segment.
- (5) By repeating steps (1)–(4) for all combinations of field nodes, the boundary of the scattered field node cloud can be obtained.

It should be noted that the value of  $\alpha$  has a big influence on the tracking accuracy of the boundary, and some experiences can be referenced. In general, for regions of convex polygons,  $\alpha$  can be larger, and for regions of concave polygons or with holes,  $\alpha$  should be smaller. The boundaries of two sets of field nodes with complex boundaries were identified using the alpha shape method and are shown in Fig. 6. It can be seen that the boundary identified by the alpha shape method reflects the shape of the problem domain well. Predictably, by using the alpha shape method, the boundary can be recognized automatically in the simulation even with severe changes in geometry. This ability enables the adaption of the method for analyzing large deformation problems.

### 3 Numerical examples

In this section, the influence of key parameters on the simulation results of the adaptive CTM–RPIM is first investigated by simulating a cantilever beam subjected to small deformations. Thereafter, the precision of the adaptive CTM–RPIM for large deformation analysis is verified by modeling cantilever beams with large deformations. Moreover, the proposed method's ability to evaluate the stability of geotechnical structures is tested using a slope and a foundation as benchmark examples. Finally, a 2-D soil collapse experiment is simulated using this method, which further demonstrates its ability to solve large deformation geotechnical problems.

#### 3.1 Discussion of the selection of key parameters

The first example considered is a cantilever beam with a downward load of parabolic distribution on the right end, as shown in Fig. 7. Both the analytical solution and the FEM result are presented as a comparison to verify the accuracy of the CTM–RPIM model. After that, four most important influential factors, regarding to the model

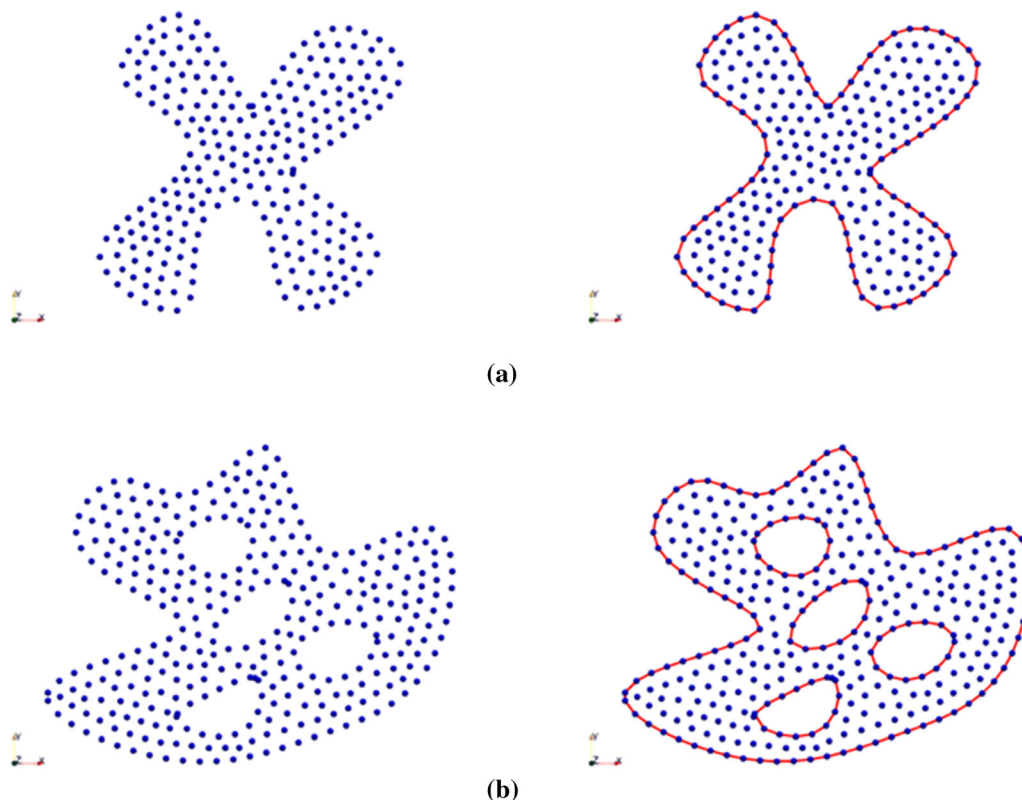


**Fig. 6** Results of boundary identification: **a** problem domain without holes; **b** problem domain with holes

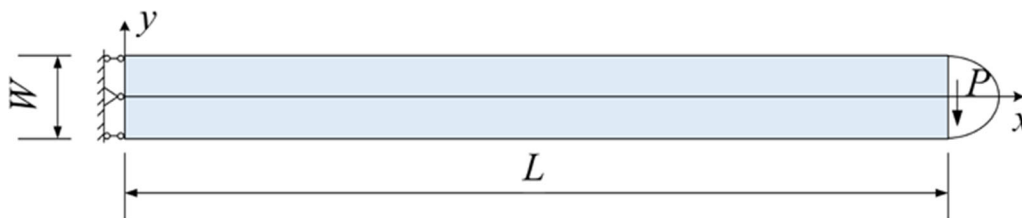


Fig. 7 The cantilever beam with a parabolic load on the right end

accuracy, are investigated; these factors are the width between two adjacent integral lines  $r_y$ , the length of the subsegment for integration  $r_x$ , the radius of the support domain  $r_c$  and the shape parameter of the RPIM  $\eta$ . To measure the distances  $r_x$ ,  $r_y$  and  $r_c$ , the mean node spacing  $d_c$  is defined as

$$d_c = \frac{\sqrt{A}}{\sqrt{n} - 1} \tag{35}$$

where  $A$  is the area of the problem domain, and  $n$  is the total number of field nodes.

The analytical solution [29, 30] to the vertical displacement is given as,

$$\Delta_y = \frac{P}{6EI} \left( 3\mu y^2(L - x) + (4 + 5\mu) \frac{W^2 x}{4} + (3L - x)x^2 \right) \tag{36}$$

where  $P$  is the force on the right end,  $E$  is Young’s modulus,  $\mu$  is Poisson’s ratio,  $W$  is the width of the beam,  $L$  is the length of the beam, and  $x$  and  $y$  are the coordinates. The values of these parameters for the simulation are shown in Table 1.

The total number of nodes used in the FEM and CTM–RPIM simulations is the same (Fig. 8). The four-node element is used in the FEM (Fig. 8a), while in the CTM–RPIM simulation, we choose  $\eta = 5.0$  and  $r_c = 2.0d_c$ , and two integration points are used for each integral subsegment. The results are shown in Fig. 9, and it can be seen that the accuracy of the CTM–RPIM is generally much higher than that of the FEM at all field node density levels because the RPIM shape functions are high order and have a larger support domain. Even when a cloud of field nodes with a loose density is used, the relative error is still low. The maximum relative error of the CTM–RPIM is only approximately 0.3%. Additionally, the integral points used

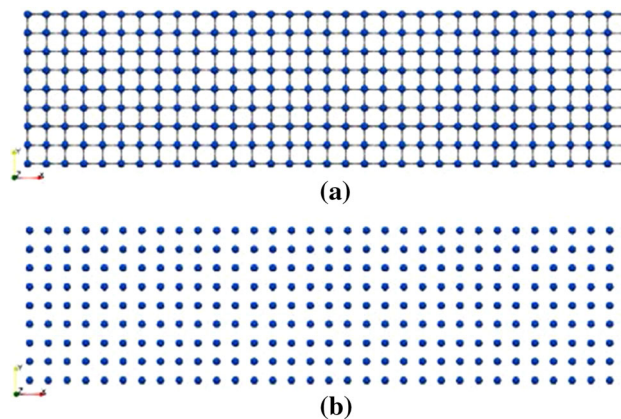


Fig. 8 FEM and CTM–RPIM models (33 × 9 nodes): a FEM model; b CTM–RPIM model

in the CTM–RPIM are less than those of the FEM. The ratio between the numbers of integration points used in the CTM–RPIM and the FEM is  $\frac{a}{2(a-1)}$ , where  $a$  is the number of nodes in the  $y$ -direction. It should be noted that the accuracy of this method is affected by many parameters, and the convergence is not monotonic under some parameter combinations, which may be caused by the high order of RPIM interpolation. In most cases of parameter combinations, the result of this method is exponentially convergent, and the accuracy is higher than that of FEM, but the accuracy may be lower than that of FEM if the parameter combination is not appropriate. Therefore, the value selection of these most influential parameters is key important, and the recommended parameter value ranges are given in the following part. As long as the parameter value is within this range, the accuracy can be guaranteed.

The influence of the number of integral points on the CTM–RPIM simulation is studied in this section. Two sets of field nodes, namely  $17 \times 5$  and  $33 \times 9$ , are used in the simulation with  $r_x = r_y = r$ . A sufficiently large radius for the support domain is selected, which is  $r_c = 4.0d_c$ . The shape parameter is set to 5.0. Only one integral point is used for each integral subsegment, which means that the number of integral points used depends on the length  $r$ . To

Table 1 The beam parameters

$P$	$E$	$\mu$	$W$	$L$
– 1000 Pa	$3 \times 10^7$ Pa	0.3	12 m	48 m

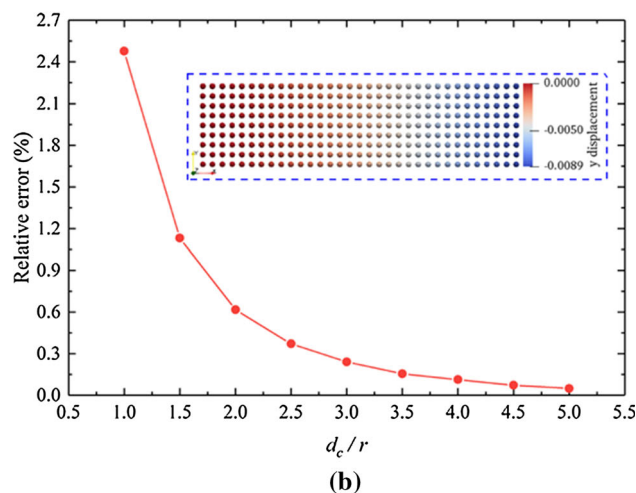
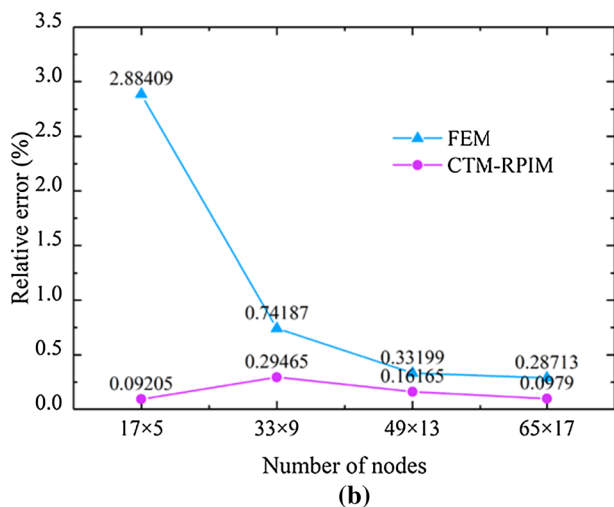
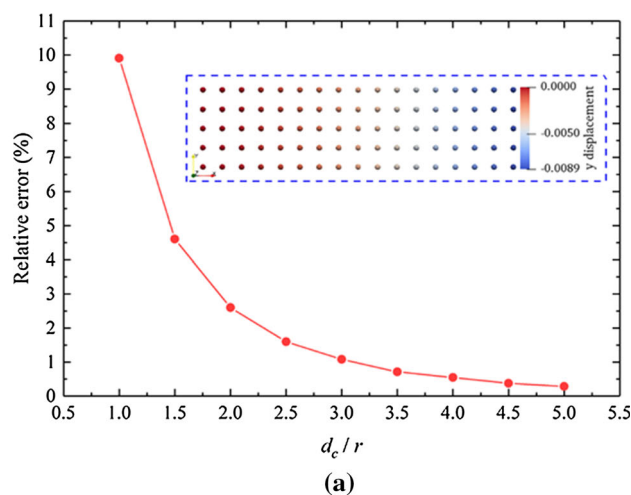
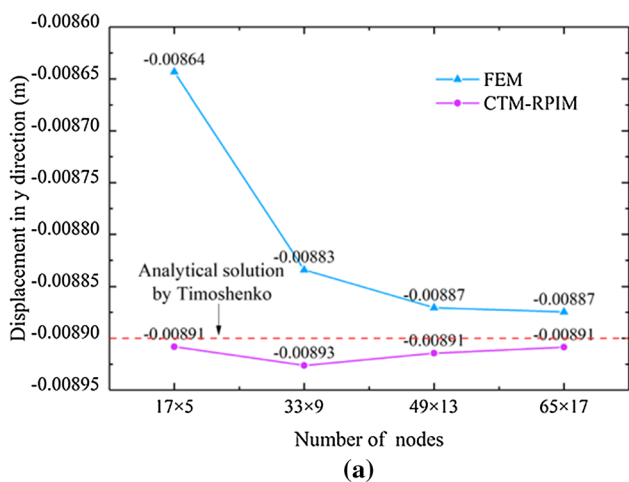


**Fig. 9** Results of vertical displacement at the right end of the cantilever beam: **a** vertical displacement at the right end of the beam; **b** relative error of the calculated vertical displacement versus the number of used nodes

**Fig. 10** The influence of  $r_x$  and  $r_y$ : **a** results of  $17 \times 5$  nodes; **b** results of  $33 \times 9$  nodes

study the influence of the integral points, the ratio  $d_c/r$  varies from 1.0 to 5.0 with an interval of 0.5. The simulation results are shown in Fig. 10. As expected, the accuracy is improved with the increase of  $d_c/r$ , and the convergence rate is roughly exponential. When  $d_c/r$  is greater than or equal to 3.0, satisfactory accuracy is obtained.

The size of the support domain is another factor that influences the CTM–RPIM simulation. A larger support domain implies that more field nodes contribute to the construction of shape functions, which leads to higher accuracy. However, the computational cost also rises because of the increase in the number of involved field nodes. Therefore, it is essential to investigate the size of the support domain in relation to the simulation accuracy and computational cost. As a circular support domain is

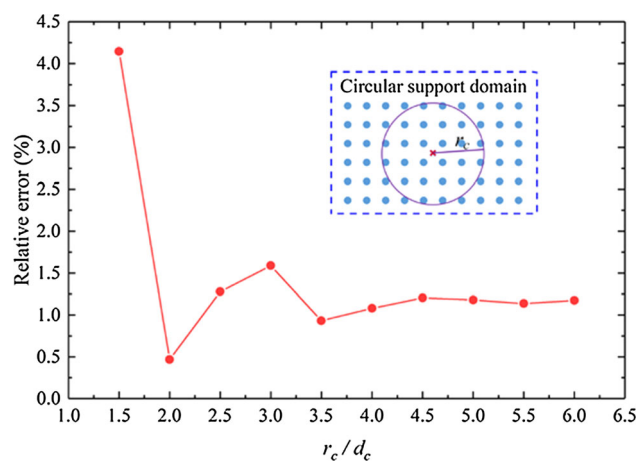


**Fig. 11** Influence of support domain radius  $r_c$

adopted in this work, the non-dimensional radius of the support domain  $r_c/d_c$  is the indicator of its size, which, in

this study, varied from 1.5 to 6.0 with an interval of 0.5. The layout of the field nodes is  $17 \times 5$ , the shape parameter  $\eta$  is set to 5.0, the distances  $r_x$  and  $r_y$  are set to  $\frac{1}{3}d_c$ , and one integral point is used for each subsegment. As shown in Fig. 11, when the radius  $r_c \geq 3.5d_c$ , the relative error is less than 1.5% and is nearly stable regardless of the increase in  $r_c/d_c$ . Therefore, the recommended range for the radius of a support domain is between  $3.5d_c$  and  $4.0d_c$ .

Finally, the effect of the shape parameter  $\eta$  from the TPS RBF on the simulation is explored. To this end, shape parameters from 1.5 to 10.5 with an interval of 1.0 are adopted in the simulation, and the other parameters are  $r_x = r_y = \frac{1}{3}d_c$  and  $r_c = 4.0d_c$ . A cloud of field nodes with a layout of  $17 \times 5$  is used to discretize the problem domain, and one integral point is assigned to each segment. Figure 12 shows that a value of  $\eta$  in the range of [3.5, 9.5] leads to higher accuracy, and the relative error is low and stable when  $\eta$  is between 4.5 and 7.5.

### 3.2 Large deformation analysis of a cantilever beam

In this section, the ability of the adaptive CTM–RPIM to address large deformation problems is demonstrated. To this end, two linear-elastic cantilever beams undergo large deformations because of the imposed force (Fig. 13) and moment (Fig. 16). The alpha shape method is used to identify the boundary of the problem domain, which makes the CTM–RPIM adaptive regardless of the change in geometry.

The first case is a cantilever beam subjected to a downward concentrated load  $P$ , as shown in Fig. 13. The length and width of the beam are  $L = 10\text{ m}$  and  $W = 1\text{ m}$ , respectively. The elastic constants are Young’s modulus  $E = 1.2\text{ GPa}$  and Poisson’s ratio  $\mu = 0.0$ . A total of 306 field

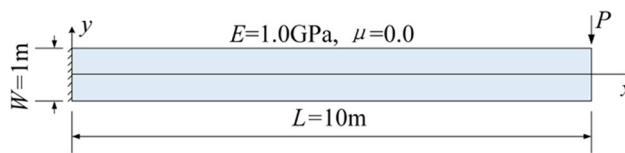


Fig. 13 Cantilever beam with concentrated force on the right end

nodes are used in the simulation. The analytical solution to this problem is available in [35].

To demonstrate the accuracy of the adaptive CTM–RPIM, a series of cases with different concentrated forces at the right-top corner are simulated with results compared to the nonlinear analytical solutions. The applied forces  $P$  are at different levels, namely 100 kN, 500 kN, 1000 kN, 1500 kN, 2000 kN, 2500 kN and 3000 kN. The curves of the tip deflection ratio  $\theta = \frac{\omega}{L}$ , where  $\omega$  is the deflection at the right end, versus the non-dimensional load parameter  $\lambda = \frac{PL^2}{EI}$ , where  $I$  is the inertia moment of the beam section, are shown in Fig. 14. The configurations of the deformed cantilever beam at concentrated force levels  $P = 2000\text{ kN}$  and  $P = 3000\text{ kN}$  are presented in Fig. 15. Clearly, the simulation results from the adaptive CTM–RPIM agree well with the analytical solution from [35], which demonstrates the correctness of the adaptive CTM–RPIM for analyzing large deformation problems.

A cantilever beam subjected to a bending moment at the right end is also studied in this section. The problem setup is shown in Fig. 16. According to the nonlinear analytical solution given by Pai and Palazotto [23], when an appropriate bending moment is applied at the right end, the cantilever beam will bend into a perfect circular ring. The bending moment  $M$  that causes the beam to achieve this state can be determined by

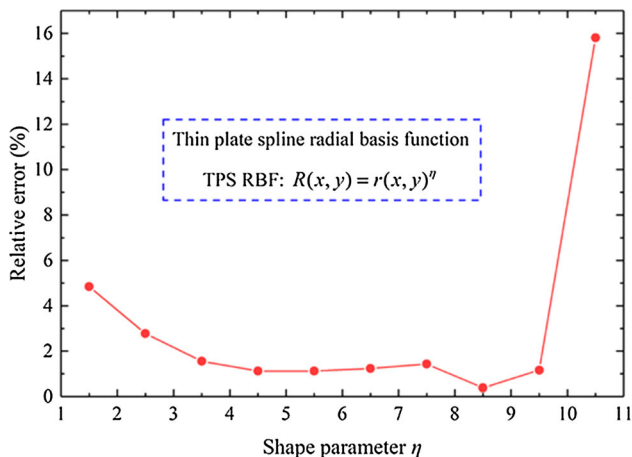


Fig. 12 Influence of shape parameter  $\eta$

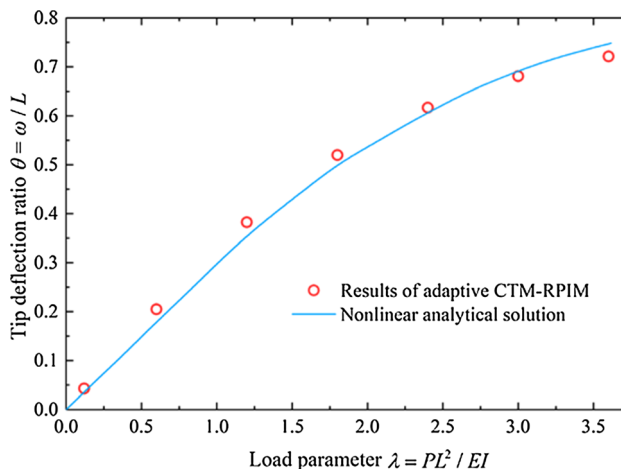
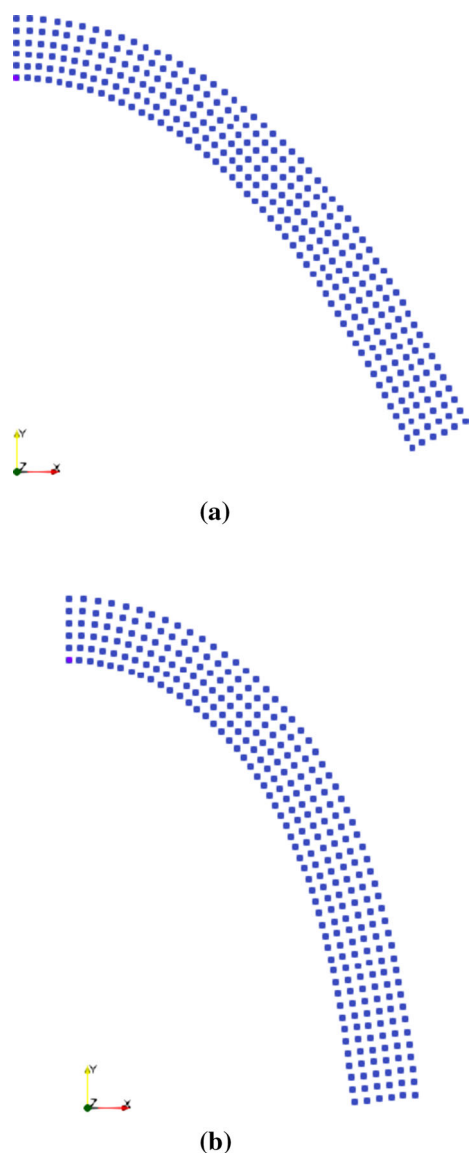
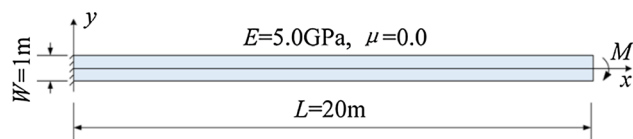


Fig. 14 Results at different levels of force  $P$



**Fig. 15** Final configuration of the beam at two different force levels: **a**  $P = 2000$  kN; **b**  $P = 3000$  kN



**Fig. 16** Cantilever beam with bending moment on the right end

$$M = \frac{2\pi EI}{L} \quad (37)$$

In the simulation, the moment is transformed into two uniform loads applied to the upper and lower halves of the

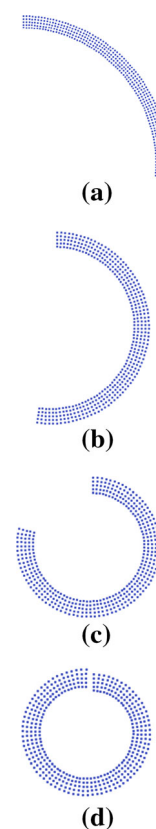


**Fig. 17** Deformation process of the beam: **a** 250 steps; **b** 500 steps; **c** 750 steps; and **d** 1000 steps

beam end section according to [33]. A total of 405 field nodes are used to discretize the problem domain, and 1000 incremental analysis steps are adopted. The deformation process of the cantilever beam obtained from the adaptive CTM–RPIM is shown in Fig. 17. A near-perfect circular ring is obtained when the moment calculated from Eq. (37) is enforced at the end of the beam, which verifies the proposed method for large deformation analysis.

### 3.3 Quasi-static analysis of the geotechnical large deformations

To evaluate the capability of the adaptive CTM–RPIM in analyzing quasi-static geotechnical large deformations, two classical benchmark examples are studied in this section. The first example evaluates the stability of a slope, and the second calculates a foundation's bearing capacity. These two examples fully demonstrate the reliability of this method for quasi-static analysis in geotechnical large deformations.

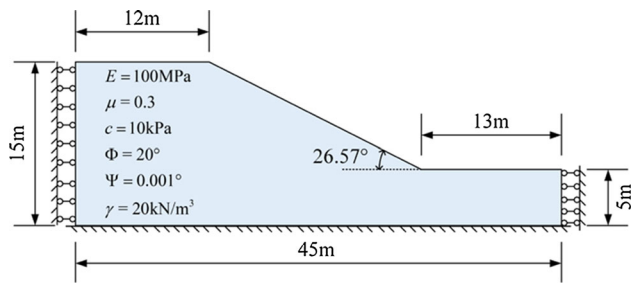


Fig. 18 Homogeneous slope

### 3.3.1 Slope stability analysis

In this section, a homogeneous soil slope is studied using the strength reduction method, and the obtained safety factor is used to verify its reliability. The geometry of the slope is provided in Fig. 18, and the material properties are Young’s modulus  $E = 100 \text{ MPa}$ , Poisson’s ratio  $\mu = 0.3$ , cohesion  $c = 10 \text{ kPa}$ , friction angle  $\Phi = 20^\circ$ , dilatancy angle  $\Psi = 0.001^\circ$  and the unit weight  $\gamma = 20 \text{ kN/m}^3$ . The bottom of the slope is fully fixed, while the lateral boundaries are fixed horizontally. The elastic-perfectly plastic constitutive model with the Mohr–Coulomb yield criterion is adopted. A total of 1881 field nodes are used in the CTM–RPIM simulation.

The formulation of the strength reduction method [19] can be expressed as

$$c' = \frac{c}{SRF} \tag{38}$$

$$\Phi' = \arctan\left(\frac{\tan(\Phi)}{SRF}\right) \tag{39}$$

where  $c'$  and  $\Phi'$  are the material parameters after strength reduction, and  $SRF$  is the reduction factor.

The reduction factor  $SRF$ , ranging from 0.8 to 1.6, is used with the simulation results after a sufficiently large step (2800 steps), as illustrated in Fig. 19a, b. Figure 19a shows that the deformation is negligible when  $SRF \leq 1.3$ . In contrast, the displacement increases continuously, and convergence cannot be achieved for  $SRF \geq 1.4$ . In other words, when  $SRF \leq 1.3$ , the slope is stable, and when  $SRF \geq 1.4$ , the slope is unstable. The same conclusion can also be obtained from the curve plotting the displacement against the  $SRF$  (see Fig. 19b). Therefore, it is clear that the slope’s safety factor  $FS$  is within (1.3, 1.4), which agrees with analytical solution 1.38 provided by Bishop and Morgenstern [5].

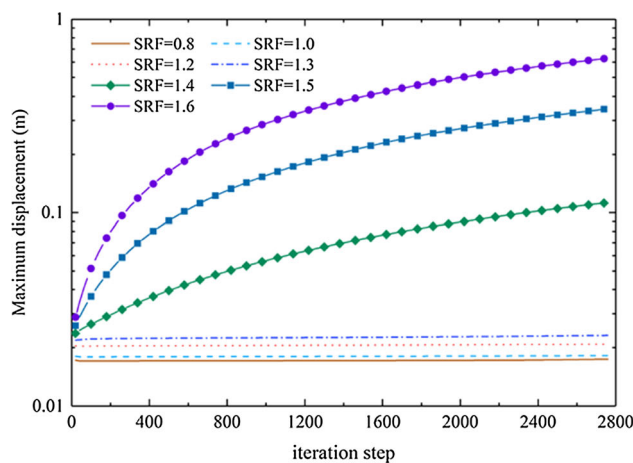
Furthermore, to gain insight into why the slope loses stability, the counterparts of the plastic strain invariant of cases  $SRF = 1.3$  and  $SRF = 1.4$  are provided in Fig. 20. When the  $SRF$  is 1.3, the plastic strain is very small, and

areas of plasticity are isolated from each other and have not penetrated the whole slope. However, when the  $SRF$  is 1.4, the plastic area is connected and forms a clear shear band, and the soil slides down along the shear band to eventually form a landslide.

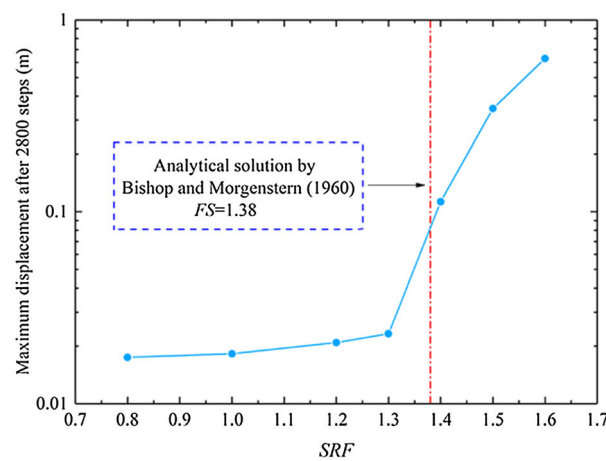
Finally, a large deformation case  $SRF = 1.6$  after 10,000 steps is provided in Fig. 21, where it can be seen that the ability of the proposed method to deal with geotechnical large deformations is; when large deformation occurs, the shear band is still clearly visible without numerical instability.

### 3.3.2 Bearing capacity analysis

A flexible strip footing on weightless soil in semi-infinite space is studied in this section, of which the bearing capacity is analyzed to test its precision, as shown in



(a)



(b)

Fig. 19 Maximum displacement of the slope: a maximum displacement for every step; b final maximum displacement after 2800 steps

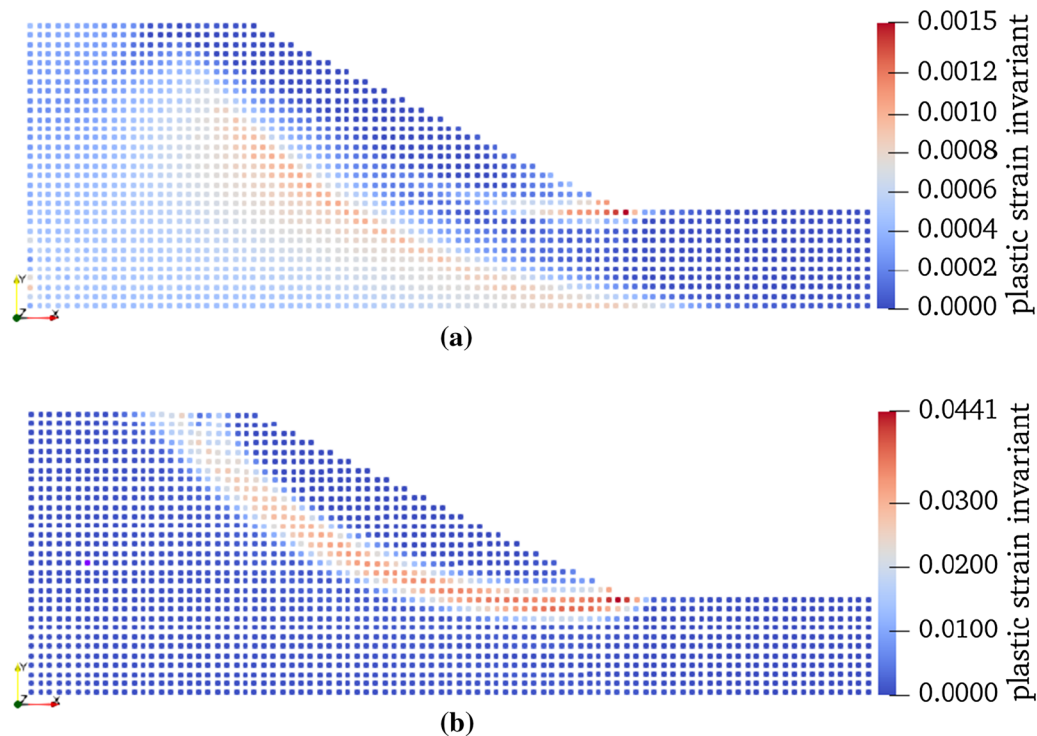


**Fig. 20** The plastic strain invariant of the slope after 2800 steps: **a**  $SRF = 1.3$ ; **b**  $SRF = 1.4$

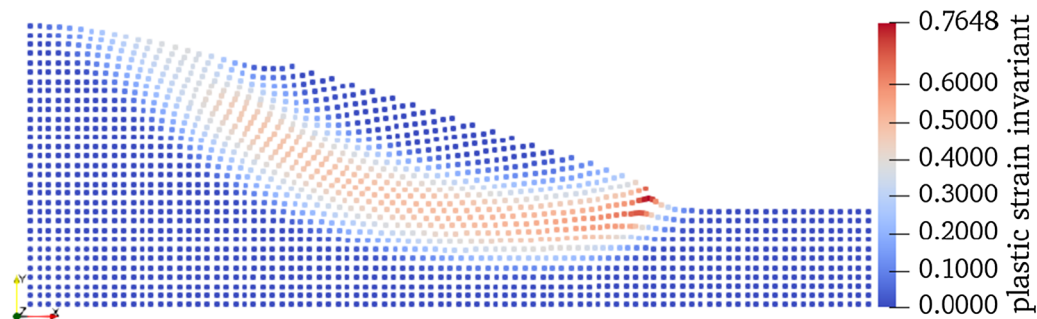


**Fig. 21** Result of  $SRF = 1.6$  after 10,000 steps

**Fig. 22a.** The analytical solution to this classical problem was found by Prandtl in 1920 [25]

$$q_{\text{failure}} = (2 + \pi)c_u \quad (40)$$

where  $c_u$  is the soil's undrained shear strength.

The simplified model is provided in Fig. 23. The scale is 12 m  $\times$  5 m, the loaded width is 2 m, and the boundary conditions are rollers at both side directions and fixed at the bottom. The elastic-perfect plastic constitutive and Mohr–Coulomb yield criterion is used in this example, and the material properties are as follows: Young's modulus  $E = 100$  MPa, Poisson's ratio  $\mu = 0.3$ , undrained cohesion  $c_u =$

100 kPa, the friction angle  $\Phi$  and dilatancy angle  $\Psi$  are both set to  $0.001^\circ$ , and the density  $\rho$  is set to  $0.0 \text{ kg/m}^3$ . A model with 1029 field nodes is generated to solve this problem, and the result is provided in Fig. 24.

At different load levels from 200 to 520 kN, convergence should occur with few iteration steps and small deformation if the strip footing is stable. As shown in Fig. 24, when the load is less than or equal to 500 kPa, convergence can be achieved quickly within 100 iteration steps, and the maximum deformation at all load levels is approximately 6 cm. However, when the load reaches

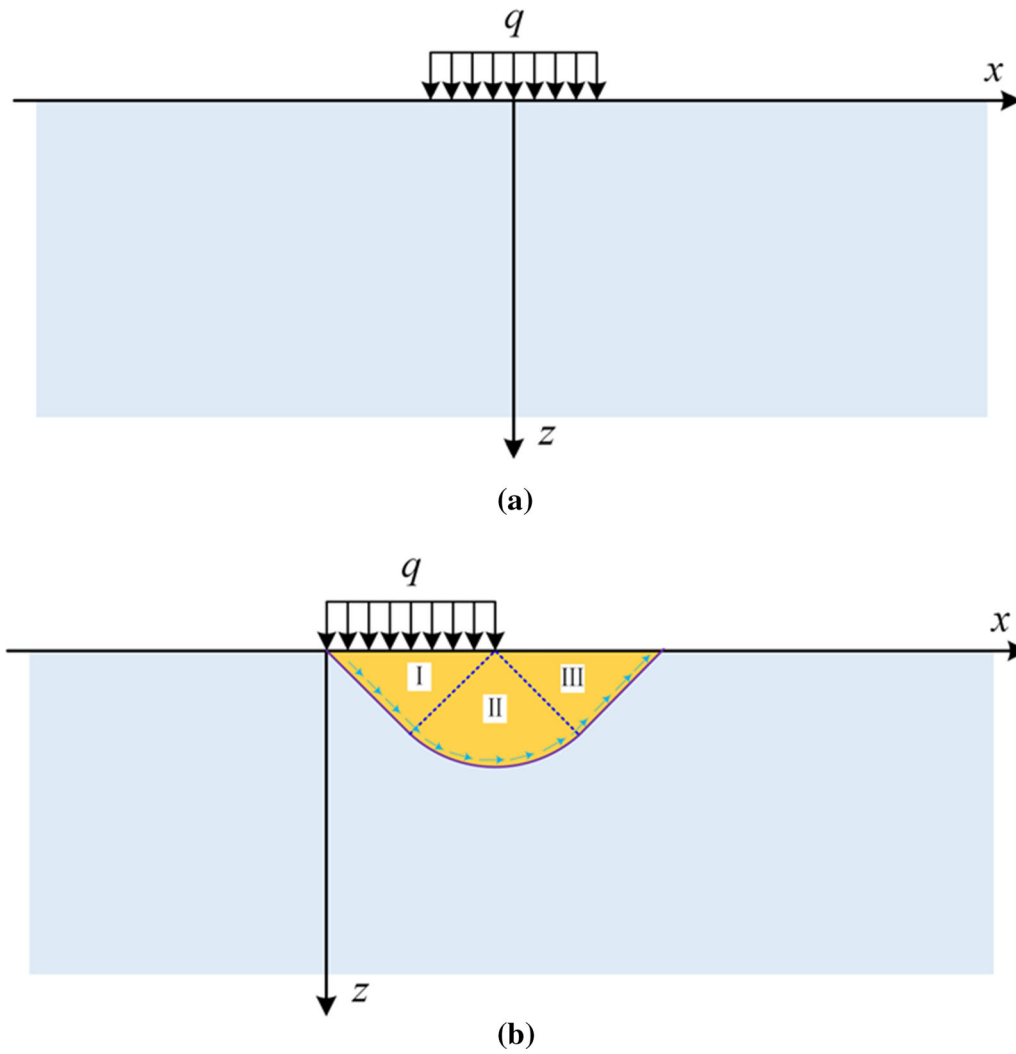


Fig. 22 Flexible strip footing on weightless soil: **a** description of the problem; **b** Prandtl's schematization [25]

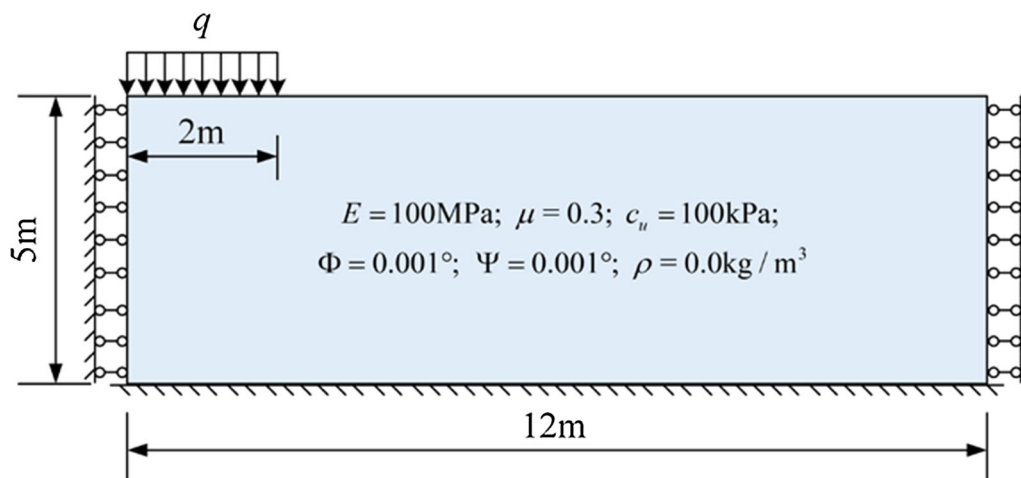


Fig. 23 Symmetry-based simplification for numerical simulation

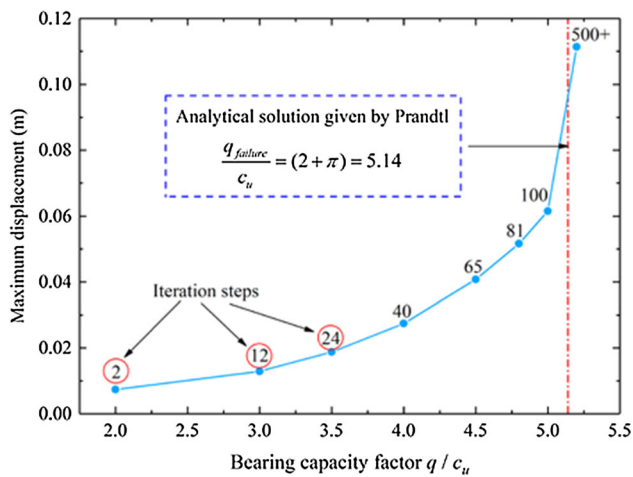


Fig. 24 Plot of the maximum displacement versus the bearing stress

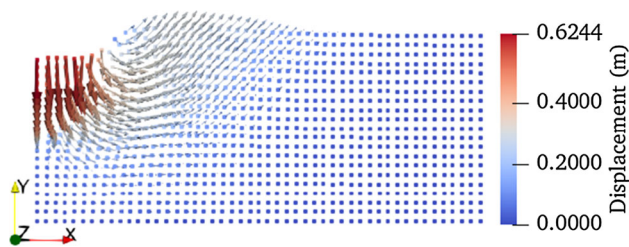


Fig. 25 Displacement at the load level of 540 kPa

520 kPa, convergence cannot be attained within 500 iterations, and the displacement at 500 steps shown in Fig. 24 is approximately 11 cm, which is nearly two times that at 500 kPa. These results indicate that the failure load of the

flexible strip footing is between 500 and 520 kPa, including Prandtl's solution of 514 kPa. That is, the adaptive CTM–RPIM is reliable when evaluating the bearing capacity of the flexible strip footing. If a more accurate result is required, a more refined numerical model can be used.

The deformed configuration at 540 kPa is provided in Fig. 25, where the deformation reaches over 0.6 m, and the failure mechanism proposed by Prandtl, shown in Fig. 22b, can be easily seen from the deformation trend displayed by the arrows with direction in Fig. 25. Again, it is verified that the adaptive CTM–RPIM has great advantages in stability evaluation and deformation trend prediction.

### 3.4 Dynamic analysis of the geotechnical large deformations

To further test the ability of this method to solve geotechnical large deformation problems, the soil collapse process was simulated. A 2-D experiment was carried out by Ha H. Bui et al. [6], where the soil particles were modeled by many small aluminum bars, as shown in Fig. 26. Constrained by a movable baffle, these bars were initially stacked into a rectangular column. At the beginning of the test, the baffle was quickly removed, and the soil column collapsed rapidly under its own weight. After a long run-out distance, it accumulated into an approximate triangular area. The soil parameters are as follows: Young's modulus  $E = 0.84$  MPa, Poisson's ratio  $\mu = 0.3$ , cohesion  $c = 0$  MPa, friction angle  $\Phi = 19.8^\circ$ , dilatancy angle  $\Psi = 0.001^\circ$  and density  $\rho = 2650$  kg/m<sup>3</sup>.

The numerical model was discretized into 1071 field nodes, and elastic-perfect plastic constitutive and Mohr–Coulomb yield criteria were used. The boundary conditions are fixed at the bottom boundary and rolling at the left

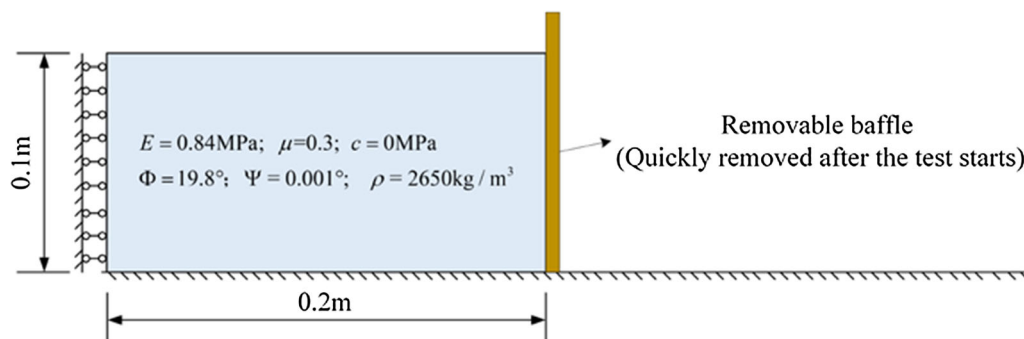
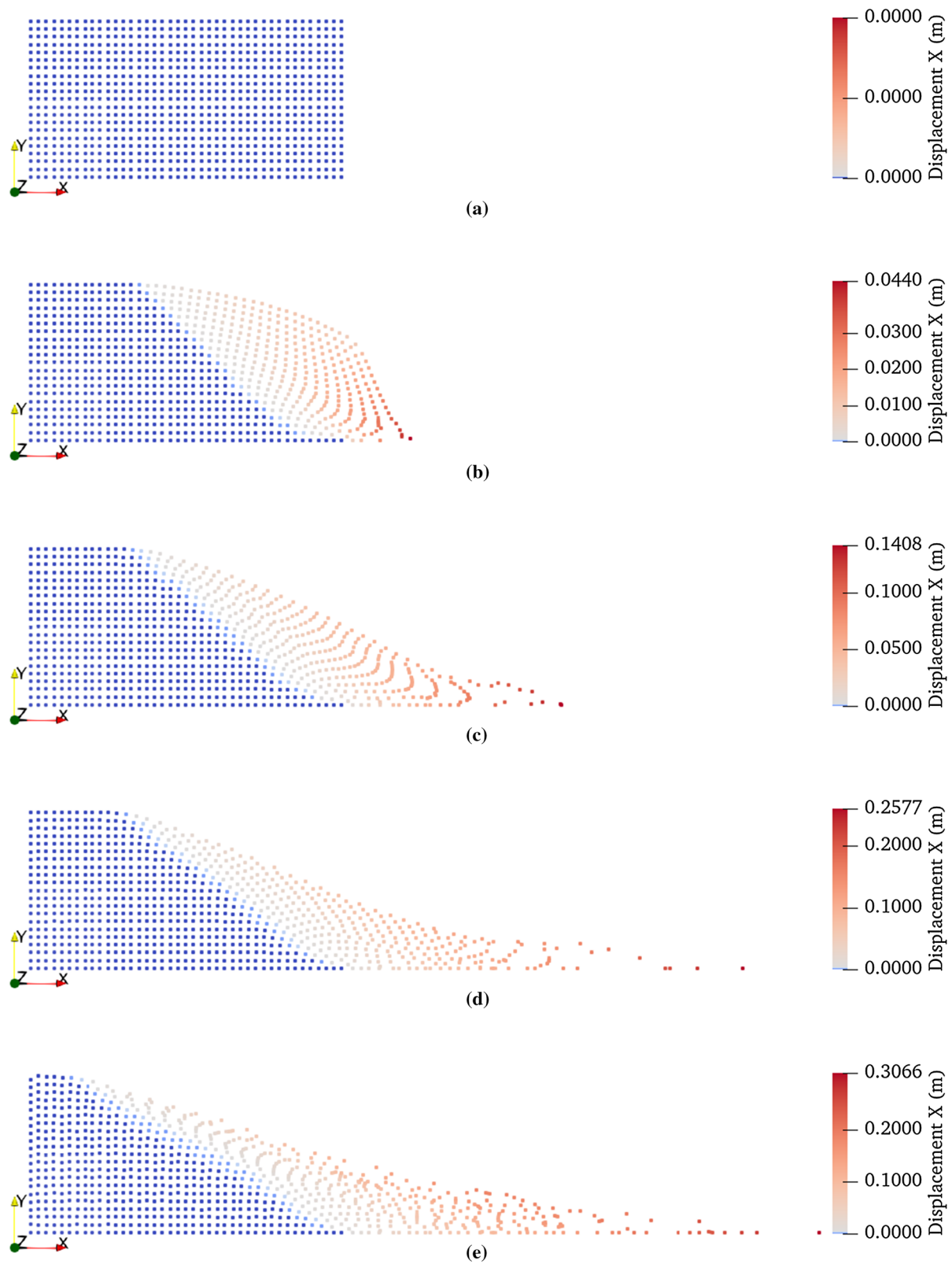


Fig. 26 2-D experiment of soil collapse [6]



**Fig. 27** Collapse process of the soil column: **a** initial configuration; **b** configuration at 0.1 s; **c** configuration at 0.2 s; **d** configuration at 0.3 s; and **e** final configuration

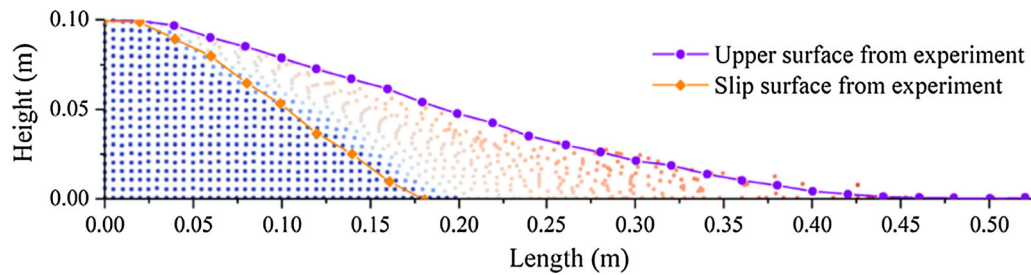


Fig. 28 Final configuration of the soil collapse example

boundary, following the settings provided in [6, 16]. Because the collapse of the soil column occurs very quickly and the deformation is extremely large, the inertia force is not negligible and the dynamic scheme is adopted here. The time step is chosen as  $\Delta t = 5.0 \mu\text{s}$ , which is small enough to ensure the stability and accuracy of the calculation.

The collapse process of the soil column is provided in Fig. 27, and the field nodes are rendered in different colors depending on the displacement to observe the deformation inside the soil column. After the baffle is removed, the soil column immediately begins to collapse, and the soil on the upper right begins to slide, while the soil on the lower-left remains static. As time progresses, the static region gradually decreases. At the end of the collapse process, the soil particles stop moving, the upper surface of the accumulation is at an angle slightly less than the friction angle, and a small region in the lower-left corner remains static. The interface between the static region and sliding region is what we call the sliding surface.

Finally, the final upper surface and the sliding surface are compared with the experimental observations, which are presented in Fig. 28. It can be clearly seen that the numerical result agrees with the experimental result, which further demonstrates the ability of the adaptive CTM–RPIM to simulate geotechnical large deformation problems.

## 4 Conclusions

An adaptive CTM–RPIM for solving geotechnical large deformation problems is introduced in this paper. Using the CTM and RPIM, the domain integration can be transformed into line integration, and the interpolation can eliminate the restraints from the background mesh. Meanwhile, to handle large deformation problems more conveniently, the alpha shape method is introduced to track the boundary automatically, and the results are shown to be accurate and convenient. To facilitate programming, both

quasi-static and dynamic versions of the computational processes are provided. Moreover, the influence of key parameters on precision is systematically explored, and the recommended values of these parameters are provided in this paper. Two geotechnical examples, slope and footing, are analyzed to demonstrate the accuracy and reliability of the method. Finally, by simulating a 2-D soil collapse experiment with a large run-out distance, the proposed method's ability to deal with large deformations is further proven. In summary, the adaptive CTM–RPIM is a promising method and has great potential in the application of large deformation geotechnical problems.

**Acknowledgements** The authors wish to acknowledge the National Natural Science Foundation of China (Grant Nos. 51979270 and 51709258) and the CAS Pioneer Hundred Talents Program for their financial support.

## References

1. Abdollahifar A, Nami MR, Shafiei AR (2012) A new MLPG method for elastostatic problems. *Eng Anal Bound Elem* 36(3):451–457
2. Ákos T, Arpad B, Gyula B, Tamas L, Arpad S, Péter G (2018) Slope stability and rockfall assessment of volcanic tuffs using RPAS with 2-D FEM slope modelling. *Nat Hazard Earth Sys* 18(2):583–597
3. Alba Y, Eduardo A, Núria P (2015) The material point method for unsaturated soils. *Géotechnique* 65(3):201–217
4. Amir K, Hematiyan M (2010) A new method for meshless integration in 2-D and 3-D Galerkin meshfree methods. *Eng Anal Bound Elem* 34:30–40
5. Bishop AW, Morgenstern NR (1960) Stability coefficients for earth slopes. *Géotechnique* 10(4):129–147
6. Bui HH, Fukagawa R, Sako K, Ohno S (2010) Lagrangian meshfree particles method (SPH) for large deformation and failure flows of geomaterial using elastic-plastic soil constitutive mode. *Int J Numer Anal Met* 32(12):1537–1570
7. Cheng L, Liu YR, Yang Q, Pan YW, Lv Z (2017) Mechanism and numerical simulation of reservoir slope deformation during impounding of high arch dams based on nonlinear FEM. *Comput Geotech* 81:143–154
8. Cruden DM (1991) A simple definition of a landslide. *B Eng Geol Environ* 43:27–29

9. Gu YT (2011) An enriched radial point interpolation method based on weak-form and strong-form. *Mech Adv Mater Struct* 18(8):578–584
10. Hematiyan M, Amir K, Liu GR (2014) A background decomposition method for domain integration in weak-form meshfree methods. *Compute Struct* 142:64–78
11. Hungr O, Leroueil S, Picarelli L (2014) The Varnes classification of landslide types, an update. *Landslides* 11(2):167–194
12. Jameel A, Harmain GA (2015) Fatigue crack growth in presence of material discontinuities by EFGM. *Int J Fatigue* 81:105–116
13. Jin YF, Yin ZY, Yuan WH (2020) Simulating retrogressive slope failure using two different smoothed particle finite element methods: a comparative study. *Eng Geol* 279:105870
14. John N (2013) Modeling imperfect interfaces in the material point method using multimaterial methods. *Cmes Comp Model Eng* 92(3):271–299
15. Li Y, Liu GR, Yue J (2018) A novel node-based smoothed radial point interpolation method for 2-D and 3-D solid mechanics problems. *Comput Struct* 196:157–172
16. Lian YP, Zhang X, Liu Y (2012) An adaptive finite element material point method and its application in extreme deformation problems. *Comput Method Appl M* 241–24:275–285
17. Liu GR, Yan L, Wang JG, Gu YT (2002) Point interpolation method based on local residual formulation using radial basis functions. *Struct Eng Mech* 14(6):713–732
18. Locat A, Leroueil S, Bernander S, Demers D, Jostad HP, Ouehb L (2011) Progressive failures in eastern Canadian and Scandinavian sensitive clays. *Can Geotech J* 48(11):1696–1712
19. Ma YC, Su PD, Li YG (2020) Three-dimensional nonhomogeneous slope failure analysis by the strength reduction method and the local strength reduction method. *Arab J Geosci* 13(2):1–7
20. Meng J, Zhang X, Utili S, Oñate E (2021) A nodal-integration based particle finite element method (N-PFEM) to model cliff recession. *Geomorphology* 381:107666
21. Meral G, Tezer-Sezgin M (2010) DRBEM solution of exterior nonlinear wave problem using FDM and LSM time integrations. *Eng Anal Bound Elem* 34(6):574–580
22. Monforte L, Arroyo M, Carbonell JM, Gens A (2017) Numerical simulation of undrained insertion problems in geotechnical engineering with the particle finite element method (PFEM). *Comput Geotech* 82:144–156
23. Pai PF, Palazotto AN (1996) Large-deformation analysis of flexible beams. *Int J Solids Struct* 33(9):1335–1370
24. Pant M, Singh IV, Mishra BK (2011) Evaluation of mixed mode stress intensity factors for interface cracks using EFGM. *App Math Model* 35(7):3443–3459
25. Prandtl L (1920) Über die Härte plastischer Körper. *Nachrichten von der Gesellschaft der Wissenschaften zu Göttingen Mathematisch-physikalische Klasse* 1920:74–85
26. Rao X, Cheng LS, Cao RY, Jiang J, Li N, Fang SD, Jia P, Wang LZ (2018) A novel green element method by mixing the idea of the finite difference method. *Eng Anal Bound Elem* 95:238–247
27. Stephen B, Ted B (1996) Nodal integration of the element-free Galerkin method. *Comput Method Appl M* 139:49–74
28. Tinesh P, Andrea B-B, Rastogi A, Eldho TI (2019) Simulation of groundwater flow in an unconfined sloping aquifer using the element-free galerkin method. *Water Resour Manag* 33(2):2827–2845
29. Xu DD, Yang YT, Zheng H, Wu AQ (2017) A high order local approximation free from linear dependency with quadrilateral mesh as mathematical cover and applications to linear elastic fractures. *Compute Struct* 178:1–16
30. Yang YT, Sun GH, Zheng H, Fu XD (2016) A four-node quadrilateral element fitted to numerical manifold method with continuous nodal stress for crack analysis. *Compute Struct* 177:69–82
31. Zahra K, Hematiyan M, Reza V (2017) Meshfree radial point interpolation method for analysis of viscoplastic problems. *Eng Anal Bound Elem* 82:172–184
32. Zhang X, Krabbenhoft K, Pedroso DM, Lyamin AV, Sheng D, da Silva MV, Wang D (2013) Particle finite element analysis of large deformation and granular flow problems. *Comput Geotech* 54:133–142
33. Zhang W, Yuan WH, Dai BB (2018) Smoothed particle finite-element method for large-deformation problems in geomechanics. *Int J Geomech* 18(4):04018010
34. Zhang W, Zhong ZH, Peng C, Yuan WH, Wu W (2021) GPU-accelerated smoothed particle finite element method for large deformation analysis in geomechanics. *Comput Geotech* 129:103856
35. Zhao GF (2014) Development of the distinct lattice spring model for large deformation analyses. *Int J Numer Anal Met* 38:1078–1100

**Publisher's Note** Springer Nature remains neutral with regard to jurisdictional claims in published maps and institutional affiliations.